Research Article

Synthesis and Mechanical Characterization of a CuMoTaWV High-Entropy Film by Magnetron Sputtering

Sajid Alvi, Dariusz M. Jarzabek, Mojtaba Gilzad Kohan, Daniel Hedman, Piotr Jenczyk, Marta Maria Natile, Alberto Vomiero, and Farid Akhtar*

Cite This: *ACS Appl. Mater. Interfaces* 2020, 12, 21070−21079

Read Online

ACCESS | Metrics & More | Article Recommendations | Supporting Information

ABSTRACT: Development of high-entropy alloy (HEA) films is a promising and cost-effective way to incorporate these materials of superior properties in harsh environments. In this work, a refractory high-entropy alloy (RHEA) film of equimolar CuMoTaWV was deposited on silicon and 304 stainless-steel substrates using DC-magnetron sputtering. A sputtering target was developed by partial sintering of an equimolar powder mixture of Cu, Mo, Ta, W, and V using spark plasma sintering. The target was used to sputter a nanocrystalline RHEA film with a thickness of ∼900 nm and an average grain size of 18 nm. X-ray diffraction of the film revealed a body-centered cubic solid solution with preferred orientation in the (110) directional plane. The nanocrystalline nature of the RHEA film resulted in a hardness of 19 ± 2.3 GPa and an elastic modulus of 259 ± 19.2 GPa. A high compressive strength of 10 ± 0.8 GPa was obtained in nanopillar compression due to solid solution hardening and grain boundary strengthening. The adhesion between the RHEA film and 304 stainless-steel substrates was increased on annealing. For the wear test against the E52100 alloy steel (Grade 25, 700−880 HV) at 1 N load, the RHEA film showed an average coefficient of friction (COF) and wear rate of 0.25 (RT) and 1.5 (300 °C), and 6.4×10^{-6} mm^3/N m (RT) and 2.5×10^{-5} mm^3/N m (300 °C), respectively. The COF was found to be 2 times lower at RT and wear rate 10^2 times lower at RT and 300 °C than those of 304 stainless steel. This study may lead to the processing of high-entropy alloy films for large-scale industrial applications.

KEYWORDS: high-entropy alloys, magnetron sputtering, spark plasma sintering, mechanical properties, wear
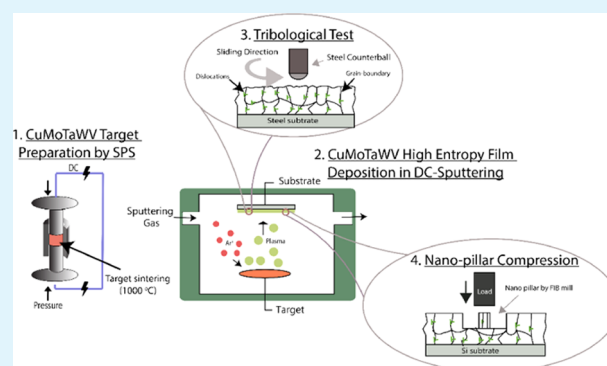
INTRODUCTION

High-entropy alloys (HEAs), since their discovery by Yeh et al. in 2004,[1] have opened up researchers to a new alloy system that contains five or more equimolar principal elements. In equimolar HEAs, each element has an equal probability of occupying the lattice sites in a crystal structure such as face-centered cubic (FCC),[2] body-centered cubic (BCC),[3] or hexagonal structure[4] crystal structures. Lattice distortion, sluggish diffusion, high entropy, and cocktail effects have been identified as the core effects contributing to the superior properties, hardness, strength, ductility, erosion, tribocorrosion, corrosion, and oxidation/wear resistance[5−7] of HEAs in a wide range of temperatures over conventional alloys. From the viewpoint of applications in extrusion dies and cutting inserts, the cost of metal powders used to develop bulk HEAs can hinder their commercialization as an alternative to the alloys in use. However, coatings of high-performance HEAs on low-cost substrates can be considered as an economically viable way forward to counter the drawbacks of the coatings employed in harsh environments, such as commercial coatings for cutting tools, extrusion dies, aerospace, and radiation resistance. Different coating techniques have been explored to deposit high-entropy coatings or films, such as laser cladding,[8,9] sputter deposition,[10−12] spraying,[13] electrochemical deposition,[14] electro-spark deposition,[15] and electron beam evaporation deposition.[16] The high hardness of high-entropy films (HEFs) renders them suitable for wear-resistant applications in aerospace, milling inserts, and biomedical applications.[17−20]

The application of HEAs at high temperatures has motivated the development of refractory high-entropy alloys (RHEAs) since 2010.[3] The reported RHEA systems of MoTaWNbV, HfNbTiZr, TaNbHfZrTi, HfMoTaTiZr, HfMoNbTaTiZr, and CuMoTaWV so far have shown improved strength, toughness, and wear resistance over a wide range of temperatures.[21−26] A few researchers have reported refractory high-entropy alloy (RHEA) films with good mechanical and electrical properties at RT.[11,27−29] Zou et al. studied micro/nanopillar compression
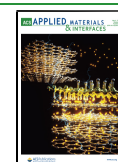
and reported an extraordinarily high yield strength of ∼10 GPa with improved ductility (∼30% compressional plastic strain) at RT for nanopillars with a diameter of 70−100 nm, and retained a yield strength of over 5 GPa up to 600 °C.[11] Feng et al. studied the effect of coating thickness and grain size on the hardness of a NbMoTaW RHEA film.[27] They reported that the highest hardness of 16 GPa was achieved at a grain size and coating thickness of 10 and 250 nm, respectively, and the hardness decreased with the increase of the grain size or thickness of the coatings. Fritz et al. studied the influence of deposition temperature during magnetron sputtering on the phase evolution of a HfNbTiVZr RHEA film.[29] It was shown that the substrate temperature, in contrast to the bulk HfNbTiVZr HEA, had a strong influence on the phase evolution and hardness of the film. The crystal structure changed from an amorphous phase with a hardness of 6.5 GPa upon RT deposition to a single-phase BCC solid solution structure with a hardness of 7.9 GPa at 275 °C substrate temperature, followed by the formation of a C14 or C15 Laves phase in the BCC matrix, and resulted in an increased hardness of 9.2 GPa at 450 °C. Kim et al. reported the effect of using a hot-pressed and conventionally sintered single target on the mechanical and electrical properties of a nanocrystalline NbMoTaW RHEA film that showed a hardness of 12 GPa.[30] However, reports on microstructural control to enhance the hardness, strength, and tribological performance of RHEA films are scarce.

Here, we report on the development of a new nanocrystalline CuMoTaWV RHEA film with high hardness, strength, and wear properties through magnetron sputtering using a single consolidated target comprising the principal elements. This work involves a novel way of making a target through partial sintering of elemental powders via the spark plasma sintering (SPS) process to lower the time and cost of processing the target material for the deposition of RHEA films. The RHEA composition has been chosen based on thermocalc simulation to obtain a mixture of a ductile FCC phase and a high-strength BCC solid solution, as reported in our previous work.[26] The addition of Cu to the refractory elements MoTaWV was done to investigate (I) the effect of lattice distortion in the films on combining Cu with refractory elements and its contribution toward the mechanical properties, and (II) the enhancement of the tribological properties of the refractory high-entropy film at RT and moderate temperatures by lowering the friction coefficient and wear rate with the formation of CuO.[31,32] Furthermore, the additions of Cu in smaller amounts and Mo to high-entropy alloys have been found to be beneficial for corrosion resistance through passivation.[33] The lattice parameters of the deposited films were verified using DFT calculations. The mechanical properties of the CuMoTaWV film were examined using nanoindentation measurements and microcompression of nanopillars. The adhesion of the deposited film on the commercial 304 stainless-steel substrate was studied and the tribological performance was verified.

■ EXPERIMENTAL SECTION

Target Preparation. The target material of CuMoTaWV with an equimolar composition was designed using thermocalc simulation. A powder mixture was made using 99.9% pure elemental Cu (10 μm, Alfa Aesar), Mo (3−7 μm, Alfa Aesar), Ta (325 mesh, US Research Nanomaterials, TX), V (325 mesh, US Research Nanomaterials, TX), and W (70 nm, US Research Nanomaterials, TX). The powders were weighed in an argon atmosphere, placed in plastic vials with the

powder mix in an equiatomic composition and Si_3N_4 milling balls in the ratio of 1:1, and ball milled for 1 h. The ball-milled powder mixture was fed into a 76 mm graphite die covered with graphite paper under an argon atmosphere, followed by transferring the die to the SPS apparatus (Dr. Sinter 2050, Sumitomo Coal Mining Co., Ltd., Japan) for consolidation. The sintering was carried out in a vacuum atmosphere at 1000 °C with a heating rate of 100 °C/min up to 800 °C, followed by a heating rate of 50 °C/min up to 1000 °C, and a soaking time of 5 min, followed by furnace cooling. A pressure of 40 MPa was used during sintering up to 900 °C, and it was then slowly decreased to 20 MPa up to 1000 °C.

Film Deposition. RHEA film deposition was carried out using DC-magnetron sputtering (Moorfield, London, UK) in an argon atmosphere. The film was deposited on a Si substrate for cross-section analysis, Rutherford backscattering spectrometry (RBS) analysis, XPS analysis, nanoindentation measurement, and nanopillar compression. The film was deposited on 304 stainless steel for X-ray diffraction (XRD) and tribological analyses. A metal sheet substrate of 304 stainless steel with a thickness of 5 mm was cut into 20 × 20 mm² and diamond-polished up to 0.4 μm, followed by cleaning with ethanol in an ultrasonicator for 30 min and drying in an oven at 80 °C for 30 min. The target material was presputtered for 5 min before deposition to remove surface oxides and contaminants. The deposition was carried out for 120 min with the substrate set to a temperature of 500 °C and a rotational speed of 8 rpm. The deposition parameters are shown in Table 1. The RHEA film deposited on 304 stainless steel was annealed at 300 °C with a heating rate of 2 °C/min in an argon atmosphere to improve the adhesion of the film.

Table 1. Sputtering Parameters for Deposition of the CuMoTaWV High-Entropy Film

substrate temperature (°C)	500
atmosphere	Ar
gas flow (sccm)	20
substrate rotation speed (rpm)	8
deposition pressure (mPa)	1.16×10^{-3}
deposition power (W)	150
deposition duration (min)	120
deposition rate (nm/min)	7.5

Film Characterization. X-ray diffraction (XRD) analysis was carried out using Cu Kα radiation in a PANalytical Empyrean (Empyrean, PANalytical, Malvern, UK) operating at 40 kV and 40 mA. Scans were performed between the 2θ range of 5 and 100° with a 10 mm divergence slit and 1° diffracted beam slits. The film composition was analyzed using Rutherford backscattering spectrometry (RBS) with a 1.8 or 2.0 MeV $^4He^+$ beam in IBM geometry. X-ray photoelectron spectra (XPS) were recorded using a PerkinElmer PHI 5600 ci spectrometer with a standard Al Kα source (1486.6 eV) working at 250 W. The working pressure was set to 5×10^{-8} Pa. The spectrometer was calibrated by assuming the binding energy (BE) of the Au $4f_{7/2}$ line to be 84.0 eV with respect to the Fermi level. Extended spectra (survey) were collected in the range 0−1300 eV (187.85 eV pass energy, 0.5 eV step, 0.025 s per step). Detailed spectra were recorded for the following regions: V 2p, Mo 3d, Ta 4f, W 4f, Cu 2p, O 1s, and C 1s (23.5 eV pass energy, 0.1 eV step, 0.2 s per step). The atomic percentage, after a Shirley-type background subtraction, was evaluated using the PHI sensitivity factors. The sample was analyzed before and after 2 min of Ar⁺ sputtering at 3.5 keV with an argon partial pressure of 5×10^{-8} mbar and a rastered area of 2.5 × 2.5 mm². The surface and cross-section morphologies of the film were studied using scanning electron microscopy (Magellan 400 XHR-SEM, FEI Company, Eindhoven, The Netherlands). The wear track morphology of the RHEA film was examined using scanning electron microscopy (SEM, JSM-IT300LV, JEOL GmbH, Germany) and energy-dispersive X-ray spectroscopy (EDS) with an accelerating voltage of 10 kV and a working distance of 10 mm. AFM measurements were performed under ambient conditions with an

Table 2. EDS Area Analysis of the CuMoTaWV Target and RHEA Film in Average Atom %

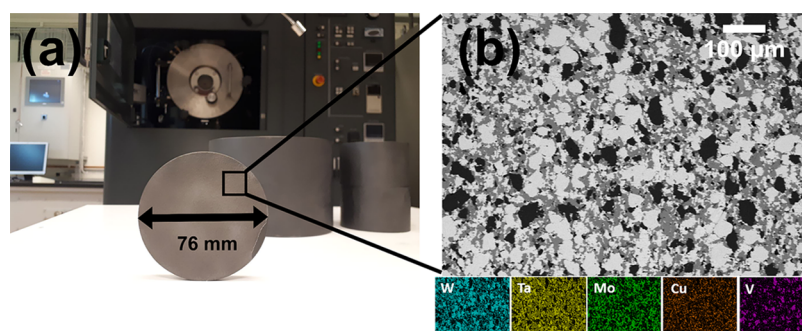| EDS	Cu	Mo	Ta	W	V	O
target	10.3 ± 0.9	30.1 ± 1.0	13.5 ± 1.5	9.0 ± 2.0	25.4 ± 1.8	11.5 ± 2.7
RHEA film	2.75 ± 0.7	23.8 ± 0.5	23 ± 0.8	23.5 ± 0.7	20.3 ± 1.2	6.5 ± 2.5

Figure 1. Preparation of a single target of CuMoTaWV: (a) SPS and (b) SEM morphology of the cross section of the target and elemental mapping.

NTEGRA AFM (NT-MDT) in semicontact mode using a polysilicon lever, monocrystal silicon probe (HA_NC series) with a tip height of 10 μm, a nominal tip radius of less than 10 nm, and a measured resonance frequency of 240.3 Hz. Nanoindentation measurements were carried out at 3 mN load using a nanoindenter (Mirco Materials, UK). The nanoindentation tests were performed at loading, unloading, and dwell times of 25, 20, and 10 s, respectively.

Tribological studies of the film were carried out at room temperature (RT) and 300 °C using 1 N normal load at a sliding speed of 0.1 m/s using a universal tribometer (Rtec Instruments, San Jose) with a ball-on-disc setup in a sliding motion. Counterballs of E52100 alloy steel (Grade 25, 700–880 HV) with diameters of 6.3 and 9.5 mm were used for RT and 300 °C tribological tests, respectively. The counterballs were cleaned with ethanol in an ultrasonicator machine for 10 min, followed by drying in an oven at 80 °C for 30 min.

A focused ion beam (FIB) was used to create four nanopillars for compression tests. For each pillar, first, a ring was etched using high current (1 nA), with the outer diameter and inner diameter set to 30 and 8 μm, respectively. This was necessary due to the fact that the flat punch used for compression tests had a diameter equal to 20 μm. Lastly, fine etching of a pillar with a current lower than 320 pA was used to mill 440-nm-diameter pillars. It has been shown that gallium ions can significantly modify the mechanical properties of the materials due to the introduction of defects and amorphization of the crystal structure.[34] However, the ions have the most significant influence on the surfaces perpendicular to the beam. In our case (milling of the pillars), the beam is parallel to the pillar's wall and the pillar's top is not exposed to the ions. We further decrease the negative influence of the ion beam by applying two steps during the milling. First, we apply a high current but, at the end, we polish the pillar with a low current (320 pA). Due to this procedure, we assume that the modified layer is not thicker than 5 nm and does not affect our results significantly.[35] The pillars were then microcompressed using an Anton Paar ultra-nanoindentation tester in load control mode with the maximum force set to 3 mN. The loading and unloading rates were set to 1 and 3 mN/min, respectively. The data acquisition rate was set to 50 Hz. The value of the compression strength was determined as the engineering strain at which 0.2% plastic deformation occurs. Young's modulus was determined from the linear fit to the data for which the value of engineering stress was less than 60% of the compression strength. Engineering stress was determined by dividing the force measured by a nanoindentation tester over the pillars' cross-section area. Hence, the pillars' diameters before and after the compression test were measured by SEM. Furthermore, to determine engineering strain, the ratio of displace-ment obtained from nanoindentation to the initial height of a pillar measured by atomic force microscopy (AFM) was obtained.

Density functional theory (DFT), as implemented in the Vienna Ab initio Simulation Package[36−39] (VASP), was used to determine the lattice parameters and mechanical properties of the CuMoTaWV HEA. Due to the disordered nature of HEAs, special quasirandom structures (SQSs) were used.[40] These were generated using the alloy theoretic automated toolkit[41] (ATAT) with a pair range of 5.5 Å and a supercell size 5 × 5 × 5 times the primitive BCC unit cell. The generated SQS contains 4 Cu, 30 Mo, 32 Ta, 31 W, and 28 V atoms, giving a composition close to that of the RHEA film given in Table 2. Calculations were performed with high accuracy using a Γ-centered 2 × 2 × 2 k-point mesh, a plane wave basis set energy cutoff equal to 600 eV, and no symmetry constraints. Methfessel–Paxton smearing of order 1 was used, with the smearing width set to 0.05 eV, and the convergence criterion for the SCF loop was set to 10^{-5} eV. The SQS was fully relaxed, both atomic positions and lattice parameters, using the conjugate-gradient algorithm until the forces acting on the structure were smaller than 0.01 eV/Å. Mechanical properties were determined from the elastic tensor, obtained using the Python Materials Genomics[42] (pymatgen) open-source Python library together with VASP. The XRD pattern for the fully relaxed SQS was simulated using Mercury Crystal Structure Visualization software[43] using a 2θ full width at half-maximum (FWHM) of 0.2°.

■ RESULTS AND DISCUSSION

A single target containing the principal elements, CuMoTaWV, was partially sintered at 1000 °C using SPS to lower the cost and time of target preparation, as shown in Figure 1. The elemental maps from the cross section of the target in Figure 1b showed a uniform distribution of all of the elemental phases. This suggests that in the DC sputter film from the single target, the plasma will evaporate all of the principal elements to the substrate. The EDS area analyses from the cross section of the target in Table 2 and Table S1 showed a uniform distribution of elements with slightly lower amounts of Cu and W.

The XRD diffractogram of the CuMoTaWV RHEA film deposited on the 304 stainless-steel substrate is shown in Figure 2, together with the simulated XRD diffractogram obtained from the DFT-optimized SQS. The as-deposited film showed the formation of a single-phase BCC solid solution with a strong (110) preferred orientation. The experimentally determined lattice parameter is 3.18 Å, which is in good agreement with the one for the DFT-optimized SQS (3.16 Å).
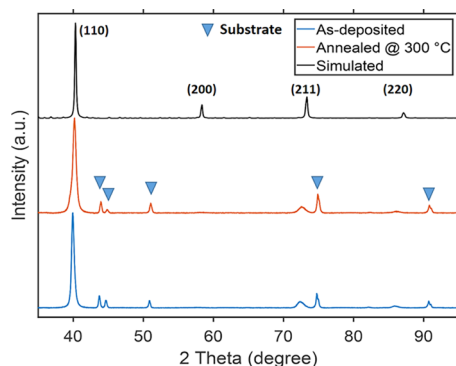
Figure 2. XRD diffractograms of as-deposited (blue, at the bottom) and 300 °C annealed (orange, in the middle) CuMoTaWV films deposited on 304 stainless-steel substrates together with the simulated XRD diffractogram (black, at the top) of the DFT-optimized SQS.

The CuMoTaWV lattice parameter is smaller than the previously reported lattice parameters of BCC RHEA films, e.g., 3.24 Å for NbMoTaW and 3.25 Å for HfNbTiVZr.[29,30] The reduced lattice constant can be related to the presence of Cu atoms having a smaller atomic radius than those of the other refractory atoms, which will reduce the lattice parameter. The grain size of the CuMoTaWV RHEA film was calculated using the Scherrer equation

$$d = \frac{k\lambda}{\beta \cos \theta}$$

where d is the grain size, k is the shape factor (0.9), λ is the wavelength (Cu $K\alpha$ = 0.154 nm), θ is the Bragg angle, and β is the full width at half-maximum (FWHM). The grain size of the as-deposited CuMoTaWV RHEA film was calculated to be 18 nm. Similar low grain sizes have been reported for RHEA films developed using a high-entropy single target, e.g., Feng et al. and Kim et al. reported average grain sizes of 10 and 15.8 nm, respectively.[27,30] In contrast, Zou et al. reported an average grain size of 150 nm for a cosputtered RHEA film using elemental targets.[11] This large difference in the grain size can be due to cosputtering from multiple targets, where sluggish diffusion is weak due to the nonhomogeneous distribution of atoms. During the sputtering of the target, atoms arriving at the substrate diffuse on the substrate to form clusters, followed by the formation of islands to lower the interfacial energy.[44] However, due to the presence of a high amount of distortion, the island growth is hindered by sluggish diffusion, one of the prime characteristics of high-entropy alloys, and leads to the formation of nanocrystalline grains.[45] The XRD analysis of the CuMoTaWV RHEA film showed no change after annealing at 300 °C in an argon atmosphere, as shown in Figure 2.

The morphologies of as-deposited films on a Si substrate and a steel substrate are shown in Figure 3 and Figure S1, respectively. The SEM analysis of the RHEA film showed a needle-like morphology, and the cross section showed a dense and textured morphology with a uniform thickness of ∼900 nm, as shown in Figure 3a,b. The initial film deposition at the film−Si substrate interface showed the formation of a dense film of ∼10 nm (Figure 3b). The initial dense deposition can be related to the formation of an amorphous film due to a lattice mismatch of ∼41% between the CuMoTaWV RHEA film (3.18 Å) and the Si crystal (5.43 Å), resulting in tremendous stress in the film. Liang et al. observed a similar interfacial microstructural evolution in TiVCrZrHf nitride
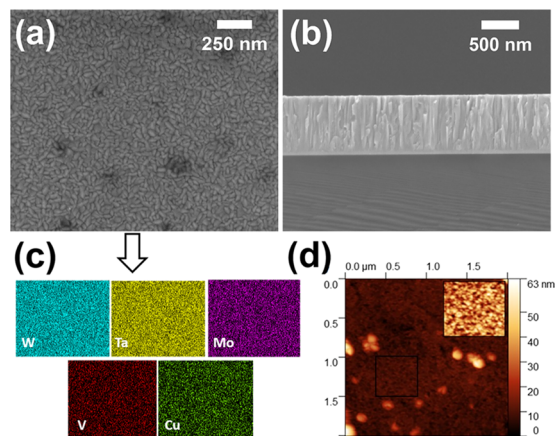

Figure 3. Characterization of a CuMoTaWV high-entropy film on a Si substrate with (a) HR-SEM plane-view surface morphology, (b) HR-SEM cross section, (c) EDS elemental mapping of the top surface, and (d) AFM analysis of the top surface.

films.[46] The EDS elemental mapping on the surface (Figure 3c) showed a uniform distribution of elements, suggesting that there was no segregation of any element/phase. The EDS area analysis of the film surface showed an equiatomic composition, except for Cu, which was found in a low amount of ∼3 atom %, as shown in Table 2 and Table S2. The low amount of Cu can be related to the high sputtering of refractory elements, which could have resulted in more scattering of Cu atoms in the sputtering plasma after initial deposition.[47] The AFM analysis showed the formation of nanocrystalline elongated grains with an average surface roughness (Sa) of 2.5 nm, as shown in Figure 3d.

The RBS measurement was carried out to observe the uniformity of composition throughout the film cross section, as shown in Figure 4. The film showed a nonhomogeneity in the in-depth composition. Specifically, the film was found to be rich in W, Ta, and Mo at the surface, while, at the substrate− film interface, the concentration of V was found to be slightly higher than those of W, Ta, Mo, and Cu, as shown in Figure 4b. The overall areal density of the film was found to be 2590 × 10^{15} at/cm^2.

XPS analysis was used to determine the chemical bonds of the CuMoTaWV film from V 2p, Mo 3d, Ta 4f, W 4f, and Cu 2p peaks, as shown in Figure 5. The carbon contamination was limited to the surface, as confirmed by the disappearance of the C photoelectron signal after a mild Ar+ sputtering. A significant decrease of C contamination is observed after 2 min of Ar$^+$ sputtering (from 67 to 19%), while complete removal of C is obtained after a further 4 min of Ar$^+$ sputtering. After sputtering, the survey profile changes significantly; the XPS peaks of metal species are more evident. The peaks' shape and positions are consistent with those reported in the literature for the corresponding metals; moreover, they do not change after 2 and 4 min of Ar$^+$ sputtering. The XPS analysis showed a uniform distribution of elements with a low amount of Cu, as shown in Table 3.

Nanoindentation measurements were carried out at a 3 mN load for 12 measurement meshes. The load versus penetration depth plot is presented in Figure 6. The penetration depth is kept below 10% of the RHEA film thickness. The film showed an average hardness of 19.5 ± 2.3 GPa and an average Young's modulus of 259.3 ± 19.2 GPa. The DFT-calculated mechanical properties showed a Young's modulus of 229 GPa, which is in
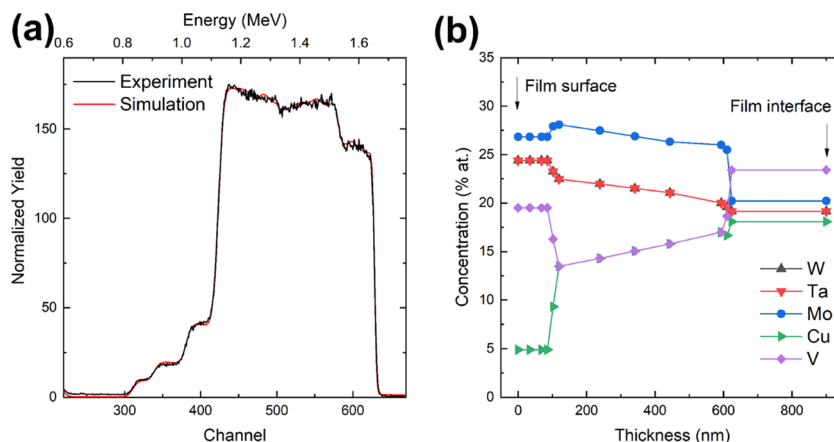
Figure 4. (a) RBS measurement and (b) elemental distribution of elements in the cross section of a CuMoTaWV high-entropy film.
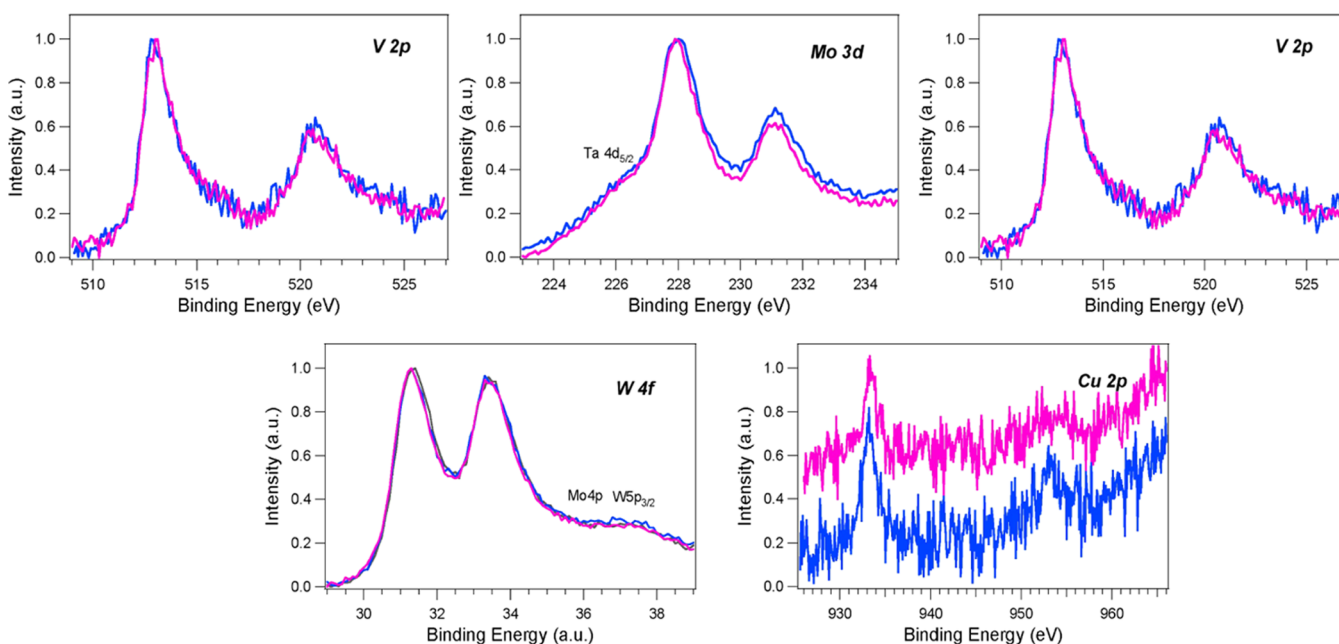

Figure 5. XPS V 2p, Mo 3d, Ta 4f, W 4f, and Cu 2p spectra of a CuMoTaWV film, deposited on Si, after 2 min of Ar$^+$ sputtering (blue line) and after 4 min of Ar$^+$ sputtering (magenta line).

Table 3. Elemental Distribution by XPS Analysis (Atom %)

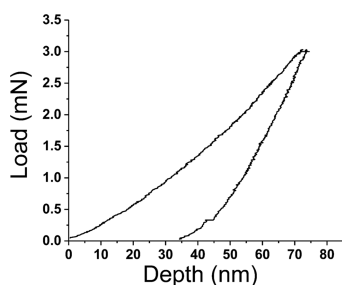|	Cu	Mo	Ta	W	V
2 min Ar$^+$ sputtering	0.7	25	29.6	27.7	17
4 min Ar$^+$ sputtering	0.8	24	29.6	27.7	17.9

Figure 6. Nanoindentation plot of load versus depth at a maximum load of 3 mN.

good agreement with the experimental nanoindentation measurements. High hardness in a metallic film can be related to the enhanced grain boundary strengthening from nanocrystallinity.[48,49] The deposited RHEA film dominates in the (110) plane due to its relatively low diffusivity with increasing film thickness as compared to the (200) and (211) planes resulting in nanocrystalline grains.[50,51] Therefore, the dislocation movement is hindered within the columnar grains during plastic deformation.[27] Furthermore, the high entropic effect, sluggish diffusion, and lattice distortion in RHEA films contribute to the measured high hardness and Young's modulus.[52] The hardness of the CuMoTaWV RHEA film is found to be higher than that of refractory metals, such as W, Ta, and Mo thin films with a hardness of 14, 11.6, and 11.8 GPa, respectively.[53−55] In general, refractory metals are found to be harder than transition metals, such as Ni and Cu, with a hardness of 6.4 and 6 GPa, respectively, due to their strong bonding and crystal structure.[56,57] The hardness of CuMoTaWV was found to be even higher than those of previously reported bulk RHEAs, such as TiHfZrTaNb, with a hardness
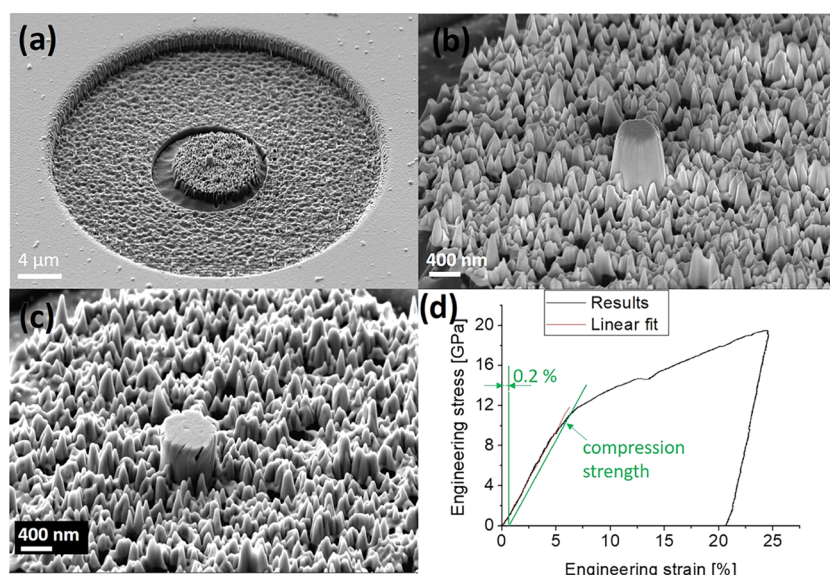
Figure 7. Nanopillar of CuMoTaWV: (a, b) before and (c) after the compression test, and (d) stress−strain plot from nanocompression.
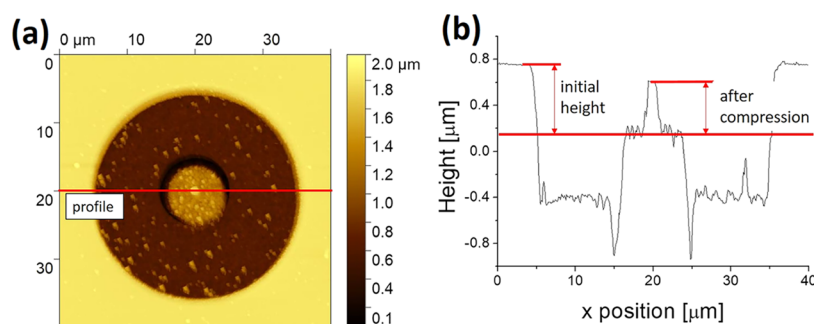

Figure 8. AFM measurement of pillar height after compression: (a) AFM analysis and (b) line profile of height versus *x*-position.
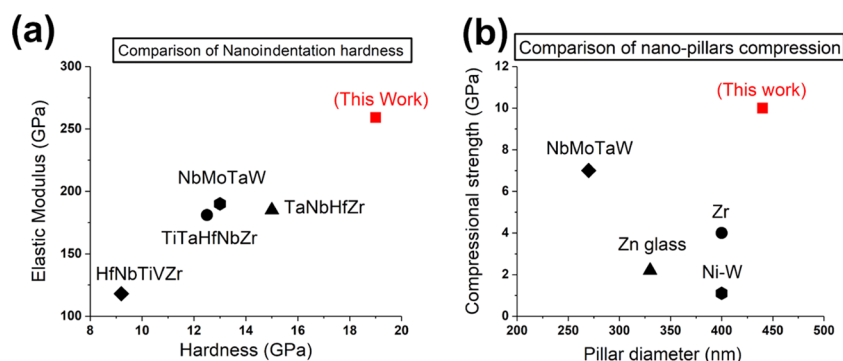

Figure 9. Comparison of the mechanical properties of a CuMoTaWV RHEA film with the literature with (a) hardness and elastic modulus and (b) pillar compressional strength versus pillar diameter.

of 4.9 GPa,[58] and RHEA films, such as NbMoTaW,[27] TaNbHfZr,[59] TiTaHfNbZr,[60] and HfNbTiVZr,[29] with a hardness of 16, 15, 12.5, and 9.2 GPa, respectively.

The nanocrystalline RHEA pillar compression of the CuMoTaWV film performed on a 440-nm-diameter pillar with an aspect ratio of 1.4 and the resulting force versus distance plot are shown in Figure 7. The nanocrystalline RHEA pillar showed a crack at the top part that propagated along the grain boundary, showing intergranular fracture behavior along the textured columnar grain film, as shown in Figure 7b,c. The nanopillar heights before and after compressional studies were calculated by AFM measurements, as shown in Figure 8. The

difference between the initial nanopillar height and that after compression was calculated to be around 200 nm (Figure 8a,b). The average yield strength and Young's modulus of the nanocrystalline RHEA pillar were calculated to be 10.7 ± 0.8 and 196 ± 10 GPa, respectively (Figure 7c). The extremely high compressional strength of the BCC HEA nanopillar has been attributed to the combined effect of a substantial solid solution hardening effect, grain size, and grain boundary strengthening.[61] Furthermore, the higher strength of the nanocrystalline RHEA CuMoTaWV film arises due to the highly columnar structure of grains in the (110) direction. Thus, the strengthening mechanism in nanopillar HEAs shifts

from dislocation-controlled to grain-boundary-controlled plastic deformation, which eventually leads to intergranular fracture. A small amount of strain burst was observed in the stress−strain plot (Figure 7d), which was related to the initiation of dislocation avalanches in the BCC solid solution in small pillars due to shear stress in the glide plane.[62,63] The reported compressive strength is among the strongest pillars reported in the literature, such as nanocrystalline NbMoTaW RHEA films (6−10 GPa),[11] nanocrystalline Ni−W alloys (~1 GPa),[64] nanocrystalline Zr pillars (~4 GPa),[65] nanolaminate Cu/Nb (~2 GPa),[66] Si (~5.3 GPa),[67] Zn-based metallic glass (~2 GPa),[68] GaN (~8 GPa),[69] and CrAlN/Si$_3$N$_4$ (16 GPa).[70] A summary of comparison of nanoindentation hardness and nanopillar compressive strength of the RHEA coating in this study with the literature is summarized in Figure 9.

The deposited high-entropy films were annealed at 300, 400, and 500 °C to increase the adhesion of the film to the 304 stainless-steel substrate. The AFM analysis of the annealed films was performed to characterize the grain morphology and resulting surface roughness, as shown in Figure 10. The
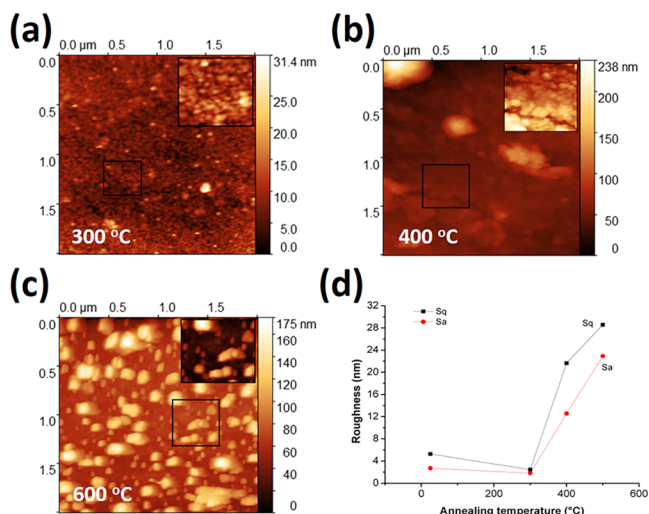

Figure 11. Friction versus sliding distance plot of as-deposited, annealed (300 °C), and 300 °C test temperature CuMoTaWV high-entropy films.

film showed an average coefficient of friction (COF) of 0.2 up to a sliding distance of 15 m, after which the COF increased to 0.7, suggesting the removal of the film from the substrate. In contrast, the wear behavior of the annealed high-entropy film showed an average COF of 0.25 up to a 30 m sliding distance, followed by a slight increase to 0.3, and remained the same until the end of the test, suggesting an improvement in the film response to wear and its adhesion to the substrate on annealing. The wear behavior at a test temperature of 300 °C showed an average COF of 1.5. The high COF at 300 °C relates to the tribochemical reaction of the RHEA film with the steel counterball, where the formation of oxides on the steel counterball can bias the frictional behavior. Furthermore, the tribological test showed low average wear rates of 6.4×10^{-6} and 2.5×10^{-5} mm^3/N m at RT and 300 °C, respectively. The frictional and wear behavior of the annealed high-entropy film can be related to its high hardness, nanocrystallinity, and better adhesion.

The SEM wear track morphology from the wear test is shown in Figure 12. The wear test of the as-deposited RHEA film showed excessive plastic deformation and smearing of the film due to low film adhesion, as shown in Figure 12a, resulting in an increase in COF. However, annealing the CuMoTaWV RHEA film at 300 °C improved the surface roughness through grain refinement and increased the adhesion of the film to the steel substrate, resulting in a steady-state average COF of 0.25, as shown in Figure 12b. The wear track from the tribological test at 300 °C showed low abrasive wear, showing the stability of the film, as shown in Figure 12c. The EDS area analysis on the wear track from the as-deposited film showed a high amount of Fe, while the wear track in the annealed film showed a low amount of Fe from the substrate, suggesting that the film was stable after the wear test of 50 m sliding distance, as shown in Table 4. The wear track from the high-temperature wear test at 300 °C showed a high amount of Cu in the wear, which can be related to the formation of CuO (Table 4).[26] The enhanced adhesion and stability of the film after annealing can be found to be beneficial for tribological applications. The use of Cu in RHEA films has been found to increase the hardness and nanopillar compressional strength compared to previously reported works on RHEA films.[11,27,29,30,59,60]

Figure 10. AFM analysis of the annealed film on the steel substrate at (a) 300 °C, (b) 400 °C, and (c) 500 °C, and (d) the resulting surface roughness (Sa and Sq) versus annealing temperature plot.

annealed CuMoTaWV film at 300 °C (Figure 10a) showed the lowest surface roughnesses of 2 nm (Sa) and 3 nm (Sq). At a higher annealing temperature of 400 °C (Figure 10b), nanocrystallinity starts to decrease, with average surface roughnesses of 12 nm (Sa) and 23 nm (Sq) (Figure 10c). Based on these findings, the RHEA film annealed at 300 °C showed the lowest surface roughness (Figure 10d) and was thus chosen to study the tribological behavior and compared with the as-deposited film. Furthermore, Vickers hardness indentation at 0.5 kgf on the as-deposited CuMoTaWV RHEA film showed radial cracks and larger crack openings in the indent as compared to the annealed (300 °C) film, indicating partial delamination, as shown in Figure S2.

The wear behavior of as-deposited and annealed CuMo-TaWV RHEA films on a 304 stainless-steel substrate against an alloy steel counterball was studied to evaluate the effect of annealing on the adhesion. The coefficient of friction versus sliding distance plot of the RHEA film from as-deposited (wear test at RT) and annealed (wear test at RT and 300 °C) films is shown in Figure 11. The wear test of the as-deposited RHEA
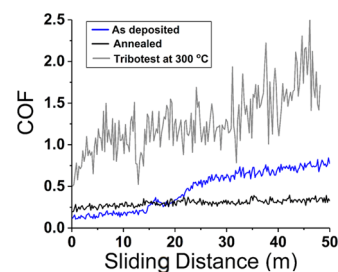
■ CONCLUSIONS

In this work, we have shown that an HEA film can be synthesized from a single partially spark-plasma-sintered target. Such use of single target sputtering was beneficial for synthesizing nanocrystalline films with low grain sizes and superior mechanical properties. The addition of Cu to the RHEA film was shown to increase the hardness and nanopillar
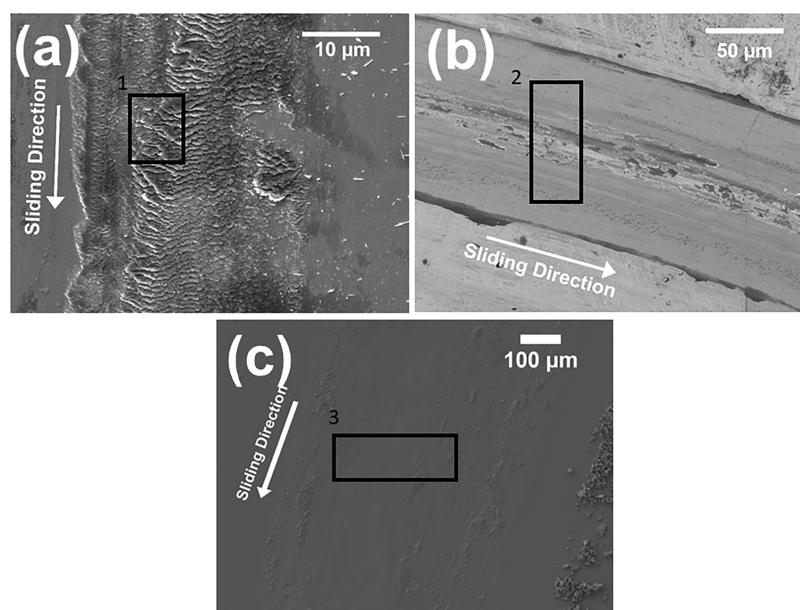
Figure 12. SEM images of wear track from (a) as-deposited film, (b) 300 °C annealed film, and (c) tribotest at 300 °C.

Table 4. EDS Area Analysis of Wear Track in Figure 12 in Average Atom %

	Cu	Mo	Ta	W	V	Fe
1	1.2	20	19	30	9.2	10
2	4.6	21.9	22.6	23	17.7	6.7
3	13.5	18.7	20.1	21.5	14.4	11.8

compressional strength. The CuMoTaWV RHEA film showed an average hardness and nanopillar compressive strength of 19 ± 2.3 and 10 ± 0.8 GPa, respectively, which are ∼20% higher than those of the reported RHEA films in the literature. The high hardness and compressional strength of the reported film were attributed to nanocrystalline grain size and grain-boundary-controlled plastic deformation. The wear behavior and adhesion of the CuMoTaWV film on a steel substrate were improved by annealing at 300 °C, and it showed improved coefficient of friction and wear resistance at RT and 300 °C. The reported results suggest that RHEA films can be beneficial for wear and nanopillar applications.

◼ ASSOCIATED CONTENT

ⓢ Supporting Information
The Supporting Information is available free of charge at https://pubs.acs.org/doi/10.1021/acsami.0c02156.

> Different characterizations of the sputtering target and film; energy-dispersive spectroscopy (EDS) data from the target; and SEM micrographs, EDS data, and Vickers indentation of the refractory high-entropy films (PDF)

◼ AUTHOR INFORMATION

Corresponding Author
Farid Akhtar − *Division of Engineering Materials, Luleå University of Technology, 97187 Luleå, Sweden;* ⓞ orcid.org/0000-0003-4888-6237; Email: farid.akhtar@ltu.se

Authors
Sajid Alvi − *Division of Engineering Materials, Luleå University of Technology, 97187 Luleå, Sweden*

Dariusz M. Jarzabek − *Department of Mechanics of Materials (ZMM), Institute of Fundamental Technological Research, Polish Academy of Sciences, 02-106 Warsaw, Poland;* ⓞ orcid.org/0000-0003-0318-1786

Mojtaba Gilzad Kohan − *Division of Experimental Physics, Luleå University of Technology, 97187 Luleå, Sweden*

Daniel Hedman − *Division of Applied Physics, Luleå University of Technology, 97187 Luleå, Sweden*

Piotr Jenczyk − *Department of Mechanics of Materials (ZMM), Institute of Fundamental Technological Research, Polish Academy of Sciences, 02-106 Warsaw, Poland*

Marta Maria Natile − *CNR—Institute of Condensed Matter Chemistry and Technologies for Energy (ICMATE), I-16149 Genoa, Italy; Department of Chemical Sciences, University of Padova, 35131 Padova, Italy;* ⓞ orcid.org/0000-0001-5591-2670

Alberto Vomiero − *Division of Experimental Physics, Luleå University of Technology, 97187 Luleå, Sweden;* ⓞ orcid.org/0000-0003-2935-1165

Complete contact information is available at:
https://pubs.acs.org/10.1021/acsami.0c02156

Notes
The authors declare no competing financial interest.

◼ ACKNOWLEDGMENTS

◼ REFERENCES

(1) Yeh, J. W.; Chen, S. K.; Lin, S. J.; Gan, J. Y.; Chin, T. S.; Shun, T. T.; Tsau, C. H.; Chang, S. Y. Nanostructured High-Entropy Alloys with Multiple Principal Elements: Novel Alloy Design Concepts and Outcomes. *Adv. Eng. Mater.* **2004**, *6*, 299−303.

(2) Zhang, L.; Zhou, Y.; Jin, X.; Du, X.; Li, B. The Microstructure and High-Temperature Properties of Novel Nano Precipitation-Hardened Face Centered Cubic High-Entropy Superalloys. *Scr. Mater.* **2018**, *146*, 226−230.

(3) Senkov, O. N.; Wilks, G. B.; Miracle, D. B.; Chuang, C. P.; Liaw, P. K. Refractory High-Entropy Alloys. *Intermetallics* **2010**, *18*, 1758−1765.

(4) Zhao, Y. J.; Qiao, J. W.; Ma, S. G.; Gao, M. C.; Yang, H. J.; Chen, M. W.; Zhang, Y. A Hexagonal Close-Packed High-Entropy Alloy: The Effect of Entropy. *Mater. Des.* **2016**, *96*, 10−15.

(5) Zhang, Y. *High-Entropy Materials, A Brief Introduction*, 1st ed.; Springer: Singapore, 2019.

(6) Huang, P.-K.; Yeh, J.-W. Effects of Nitrogen Content on Structure and Mechanical Properties of Multi-Element (AlCrNbSiTiV)N Coating. *Surf. Coat. Technol.* **2009**, *203*, 1891−1896.

(7) Ayyagari, A. V.; Gwalani, B.; Muskeri, S.; Mukherjee, S.; Banerjee, R. Surface Degradation Mechanisms in Precipitation-Hardened High-Entropy Alloys. *npj Mater. Degrad.* **2018**, *2*, 33.

(8) Zhang, M.; Zhou, X.; Yu, X.; Li, J. Synthesis and Characterization of Refractory TiZrNbWMo High-Entropy Alloy Coating by Laser Cladding. *Surf. Coat. Technol.* **2017**, *311*, 321−329.

(9) Ley, N.; Joshi, S. S.; Zhang, B.; Ho, Y. H.; Dahotre, N. B.; Young, M. L. Laser Coating of a CrMoTaWZr Complex Concentrated Alloy onto a H13 Tool Steel Die Head. *Surf. Coat. Technol.* **2018**, *348*, 150−158.

(10) Chang, H. W.; Huang, P. K.; Yeh, J. W.; Davison, A.; Tsau, C. H.; Yang, C. C. Influence of Substrate Bias, Deposition Temperature and Post-Deposition Annealing on the Structure and Properties of Multi-Principal-Component (AlCrMoSiTi)N Coatings. *Surf. Coat. Technol.* **2008**, *202*, 3360−3366.

(11) Zou, Y.; Ma, H.; Spolenak, R. Ultrastrong Ductile and Stable High-Entropy Alloys at Small Scales. *Nat. Commun.* **2015**, *6*, 1−8.

(12) Yalamanchili, K.; Wang, F.; Schramm, I. C.; Andersson, J. M.; Johansson Jöesaar, M. P.; Tasnádi, F.; Mücklich, F.; Ghafoor, N.; Odén, M. Exploring the High Entropy Alloy Concept in (AlTiVNbCr)N. *Thin Solid Films* **2017**, *636*, 346−352.

(13) Panagopoulou, M.; Vernardou, D.; Koudoumas, E.; Katsarakis, N.; Tsoukalas, D.; Raptis, Y. S. Tunable Properties of Mg-Doped V2O5 Thin Films for Energy Applications: Li-Ion Batteries and Electrochromics. *J. Phys. Chem. C* **2017**, *121*, 70−79.

(14) Yao, C.; Wei, B.; Zhang, P.; Lu, X.; Liu, P.; Tong, Y. Facile Preparation and Magnetic Study of Amorphous Tm-Fe-Co-Ni-Mn Multicomponent Alloy Nanofilm. *J. Rare Earths* **2011**, *29*, 133−137.

(15) Li, Q. H.; Yue, T. M.; Guo, Z. N. Electro-Spark Deposition of Multi-Element High Entropy Alloy Coating. *ASM International, Member/Customer Service Center Materials* **2010**, *3*, 1538−1547.

(16) Yue, T. M.; Xie, H.; Lin, X.; Yang, H.; Meng, G. Microstructure of Laser Re-Melted AlCoCrCuFeNi High Entropy Alloy Coatings Produced by Plasma Spraying. *Entropy* **2013**, *15*, 2833−2845.

(17) Zhu, G.; Liu, Y.; Ye, J. Fabrication and Properties of Ti (C, N) -Based Cermets with Multi-Component AlCoCrFeNi High-Entropy Alloys Binder. *Mater. Lett.* **2013**, *113*, 80−82.

(18) de la Obra, A. G.; Avilés, M. A.; Torres, Y.; Chicardi, E.; Gotor, F. J. A New Family of Cermets: Chemically Complex but Microstructurally Simple. *Int. J. Refract. Met. Hard Mater.* **2017**, *63*, 17−25.

(19) Linder, D.; Holmström, E.; Norgren, S. High Entropy Alloy Binders in Gradient Sintered Hardmetal. *Int. J. Refract. Met. Hard Mater.* **2018**, *71*, 217−220.

(20) Holmström, E.; Lizárraga, R.; Linder, D.; Salmasi, A.; Wang, W.; Kaplan, B.; Mao, H.; Larsson, H.; Vitos, L. High Entropy Alloys: Substituting for Cobalt in Cutting Edge Technology. *Appl. Mater. Today* **2018**, *12*, 322−329.

(21) Senkov, O. N.; Wilks, G. B.; Scott, J. M.; Miracle, D. B. Mechanical Properties of Nb25Mo25Ta25W25 and V20Nb20Mo20-Ta20W20 Refractory High Entropy Alloy. *Intermetallics* **2011**, *19*, 698−706.

(22) Senkov, O. N.; Scott, J. M.; Senkova, S. V.; Meisenkothen, F.; Miracle, D. B.; Woodward, C. F. Microstructure and Elevated Temperature Properties of a Refractory TaNbHfZrTi Alloy. *J. Mater. Sci.* **2012**, *47*, 4062−4074.

(23) Yao, H. W.; Qiao, J. W.; Gao, M. C.; Hawk, J. A.; Ma, S. G.; Zhou, H. F.; Zhang, Y. NbTaV-(Ti,W) Refractory High-Entropy Alloys: Experiments and Modeling. *Mater. Sci. Eng. A* **2016**, *674*, 203−211.

(24) Soni, V.; Senkov, O. N.; Gwalani, B.; Miracle, D. B.; Banerjee, R. Microstructural Design for Improving Ductility of An Initially Brittle Refractory High Entropy Alloy. *Sci. Rep.* **2018**, *8*, No. 8816.

(25) Poulia, A.; Georgatis, E.; Lekatou, A.; Karantzalis, A. Dry-Sliding Wear Response of MoTaWNbV High Entropy Alloy. *Adv. Eng. Mater.* **2017**, *19*, No. 1600535.

(26) Alvi, S.; Akhtar, F. High Temperature Tribology of CuMoTaWV High Entropy Alloy. *Wear* **2019**, *426−427*, 412−419.

(27) Feng, X. B.; Zhang, J. Y.; Wang, Y. Q.; Hou, Z. Q.; Wu, K.; Liu, G.; Sun, J. Size Effects on the Mechanical Properties of Nanocrystalline NbMoTaW Refractory High Entropy Alloy Thin Films. *Int. J. Plast.* **2017**, *95*, 264−277.

(28) Feng, X.; Zhang, J.; Xia, Z.; Fu, W.; Wu, K.; Liu, G.; Sun, J. Stable Nanocrystalline NbMoTaW High Entropy Alloy Thin Films with Excellent Mechanical and Electrical Properties. *Mater. Lett.* **2018**, *210*, 84−87.

(29) Fritze, S.; Koller, C. M.; Fieandt, L.; Von; Malinovskis, P.; Johansson, K.; Lewin, E.; Mayrhofer, P. H.; Jansson, U. Influence of Deposition Temperature on the Phase Evolution of HfNbTiVZr High-Entropy Thin Films. *Materials* **2019**, 10−17.

(30) Kim, H.; Nam, S.; Roh, A.; Son, M.; Ham, M.; Kim, J.; Choi, H. Mechanical and Electrical Properties of NbMoTaW Refractory High-Entropy Alloy Thin Films. *Int. J. Refract. Metals Hard Mater.* **2019**, *80*, 286−291.

(31) Goto, M.; Kasahara, A.; Tosa, M. Low Frictional Property of Copper Oxide Thin Films Optimised Using a Combinatorial Sputter Coating System. *Appl. Surf. Sci.* **2006**, *252*, 2482−2487.

(32) Torres, H.; Ripoll, M. R.; Prakash, B. Tribological Behaviour of Self-Lubricating Materials at High Temperatures. *Int. Mater. Rev.* **2018**, *63*, 309−340.

(33) Qiu, Y.; Thomas, S.; Gibson, M. A.; Fraser, H. L.; Birbilis, N. Corrosion of High Entropy Alloys. *npj Mater. Degrad.* **2017**, *1*, 15.

(34) Bei, H.; Shim, S.; Miller, M. K.; Pharr, G. M.; George, E. P. Effects of Focused Ion Beam Milling on the Nanomechanical Behavior of a Molybdenum-Alloy Single Crystal. *Appl. Phys. Lett.* **2007**, *91*, No. 111915.

(35) Singh, S.; Kaira, C. S.; Bale, H.; Huynh, C.; Merkle, A.; Chawla, N. In Situ Micropillar Compression of Al/SiC Nanolaminates Using Laboratory- Based Nanoscale X-Ray Microscopy: Effect of Nanopores on Mechanical Behavior. *Mater. Charact.* **2019**, *150*, 207−212.

(36) Perdew, J. P.; Burke, K.; Ernzerhof, M. Generalized Gradient Approximation Made Simple. *Phys. Rev. Lett.* **1996**, *77*, 3865−3868.

(37) Kresse, G.; Joubert, D. From Ultrasoft Pseudopotentials to the Projector Augmented-Wave Method. *Phys. Rev. B* **1999**, *59*, 1758−1775.

(38) Kresse, G.; Furthmüller, J. Efficiency of Ab-Initio Total Energy Calculations for Metals and Semiconductors Using a Plane-Wave Basis Set. *Comput. Mater. Sci.* **1996**, *6*, 15−50.

(39) Kresse, G.; Furthmüller, J. Efficient Iterative Schemes for Ab Initio Total-Energy Calculations Using a Plane-Wave Basis Set. *Phys. Rev. B* **1996**, *54*, 11169−11186.

(40) Zunger, A.; Wei, S.-H.; Ferreira, L. G.; Bernard, J. E. Special Quasirandom Structures. *Phys. Rev. Lett.* **1990**, *65*, 353−356.

(41) van de Walle, A.; Tiwary, P.; de Jong, M.; Olmsted, D. L.; Asta, M.; Dick, A.; Shin, D.; Wang, Y.; Chen, L.-Q.; Liu, Z.-K. Efficient Stochastic Generation of Special Quasirandom Structures. *Calphad* **2013**, *42*, 13−18.

(42) Ong, S. P.; Richards, W. D.; Jain, A.; Hautier, G.; Kocher, M.; Cholia, S.; Gunter, D.; Chevrier, V. L.; Persson, K. A.; Ceder, G. Python Materials Genomics (Pymatgen): A Robust, Open-Source Python Library for Materials Analysis. *Comput. Mater. Sci.* **2013**, *68*, 314−319.

(43) Macrae, C. F.; Bruno, I. J.; Chisholm, J. A.; Edgington, P. R.; McCabe, P.; Pidcock, E.; Rodriguez-Monge, L.; Taylor, R.; van de Streek, J.; Wood, P. A. Mercury CSD 2.0-0new Features for the Visualization and Investigation of Crystal Structures. *J. Appl. Crystallogr.* **2008**, *41*, 466−470.

(44) Reichelt, K. Nucleation and Growth of Thin Films. *Vacuum* **1988**, *38*, 1083−1099.

(45) Ng, C.; Guo, S.; Luan, J.; Shi, S.; Liu, C. T. Entropy-Driven Phase Stability and Slow Diffusion Kinetics in an Al0.5CoCrCuFeNi High Entropy Alloy. *Intermetallics* **2012**, *31*, 165−172.

(46) Liang, S. C.; Chang, Z. C.; Tsai, D. C.; Lin, Y. C.; Sung, H. S.; Deng, M. J.; Shieu, F. S. Effects of Substrate Temperature on the Structure and Mechanical Properties of (TiVCrZrHf)N Coatings. *Appl. Surf. Sci.* **2011**, *257*, 7709−7713.

(47) Särhammar, E.; Strandberg, E.; Martin, N.; Nyberg, T. Sputter Rate Distribution and Compositional Variations in Films Sputtered from Elemental and Multi-Element Targets at Different Pressures. *Int. J. Mater. Sci. Appl.* **2014**, *3*, 29−36.

(48) Ovid'Ko, I. A.; Valiev, R. Z.; Zhu, Y. T. Review on Superior Strength and Enhanced Ductility of Metallic Nanomaterials. *Prog. Mater. Sci.* **2018**, *94*, 462−540.

(49) Petch, N. J. The Cleavage Strength of Polycrystals. *J. Iron Steel Inst., London* **1953**, *173*, 25−28.

(50) Wang, X.; Wu, Z.; Hou, Q. Effects of Temperature and Surface Orientation on Migration Behaviours of Helium Atoms near Tungsten Surfaces. *J. Nucl. Mater.* **2015**, *465*, 455−463.

(51) Bassett, D. W.; Parsley, M. J. Field Ion Microscope Studies of Transition Metal Adatom Diffusion on (110), (211) and (321) Tungsten Surfaces. *J. Phys. D: Appl. Phys.* **1970**, *3*, 707−716.

(52) Yeh, J. W. Recent Progress in High-Entropy Alloys. *Ann. Chim. Sci. Mater.* **2006**, *31*, 633−648.

(53) Saha, R.; Nix, W. Soft Films on Hard Substrate - Nanoindentation of Tungesten Films on Sapphire Substrates. *Mater. Sci. Eng. A* **2001**, *319−321*, 898−901.

(54) Zhang, M.; Yang, B.; Chu, J.; Nieh, T. Hardness Enhancement in Nanocrystalline Tantulum Thin Films. *Scr. Mater.* **2006**, *54*, 1227−1230.

(55) Yoder, K. B.; Elmustafa, A. A.; Lin, J. C.; Hoffman, R.; et al. Activation Analysis of Deformation in Evaporated Molybdenum Thin Films. *J. Phys. D: Appl. Phys.* **2003**, *36*, 884.

(56) Schuh, C. A.; Nieh, T. G.; Ymasaki, T. Hall-Petch Breakdown Manifested in Abrasive Wear Resistance of Nanocrystalline Nickel. *Scr. Mater.* **2002**, *46*, 735−740.

(57) Beegan, D.; Chowdhury, S.; Laugier, M. T. Work of Indentation Methods for Determining Copper Film Hardness. *Surf. Coat. Technol.* **2005**, *192*, 57−63.

(58) Dirras, G.; Lilensten, L.; Djemia, P.; Laurent-brocq, M.; Tingaud, D.; Couzinié, J.; Perriere, L.; Chauveau, T.; Guillot, I. Elastic and Plastic Properties of as-Cast Equimolar TiHfZrTaNb High-Entropy Alloy. *Mater. Sci. Eng. A* **2016**, *654*, 30−38.

(59) Song, B.; Li, Y.; Cong, Z.; Li, Y.; Song, Z.; Chen, J. Effects of Deposition Temperature on the Nanomechanical Properties of Refractory High Entropy TaNbHfZr Films. *J. Alloys Compd.* **2019**, *797*, 1025−1030.

(60) Tüten, N.; Canadinc, D.; Motallebzadeh, A.; Bal, B. Intermetallics Microstructure and Tribological Properties of Ti-TaHfNbZr High Entropy Alloy Coatings Deposited on Ti E 6Al E 4V Substrates. *Intermetallics* **2019**, *105*, 99−106.

(61) Zou, Y. Nanomechanical Studies of High-Entropy Alloys. *J. Mater. Res.* **2018**, *33*, 3035−3054.

(62) Brinckmann, S.; Kim, J.; Greer, J. R. Fundamental Differences in Mechanical Behavior between Two Types of Crystals at the Nanoscale. *Phys. Rev. Lett.* **2008**, No. 155502.

(63) Schneider, A. S.; Frick, C. P.; Clark, B. G.; Gruber, P. A.; Arzt, E. Influence of Orientation on the Size Effect in Bcc Pillars with Different Critical Temperatures. *Mater. Sci. Eng. A* **2011**, *528*, 1540−1547.

(64) Jang, D.; Greer, J. R. Size-Induced Weakening and Grain Boundary-Assisted Deformation in 60 Nm Grained Ni Nanopillars. *Scr. Mater.* **2011**, *64*, 77−80.

(65) Zhang, J. Y.; Cui, J. C.; Liu, G.; Sun, J. Deformation Crossover in Nanocrystalline Zr Micropillars: The Strongest External Size. *Scr. Mater.* **2013**, *68*, 639−642.

(66) Mara, N. A.; Bhattacharyya, D.; Dickerson, P.; Hoagland, R. G.; Misra, A. Deformability of Ultrahigh Strength Nanolayered 5 Nm Cu/Nb Nanolayered Composites. *Appl. Phys. Lett.* **2008**, No. 231901.

(67) Rzepiejewska-malyska, K.; Leifer, K.; Hale, M.; Tang, Y.; Ballarini, R.; Gerberich, W. W.; Michler, J. Brittle-to-Ductile Transition in Uniaxial Compression of Silicon Pillars at Room Temperature. *Adv. Funct. Mater.* **2009**, 2439−2444.

(68) Jang, D.; Greer, J. R. Transition from a Strong-yet-Brittle to a Stronger-and-Ductile State by Size Reduction of Metallic Glasses. *Nat. Mater.* **2010**, *9*, 215−219.

(69) Wheeler, J. M.; Niederberger, C.; Tessarek, C.; Christiansen, S.; Michler, J. Extraction of Plasticity Parameters of GaN with High Temperature, in Situ Micro-Compression. *Int. J. Plast.* **2013**, *40*, 140−151.

(70) Liu, S.; Raghavan, R.; Zeng, X. T.; Michler, J.; Clegg, W. J. Compressive Deformation and Failure of CrAlN/Si3N4 Nano-composite Coatings. *Appl. Phys. Lett.* **2014**, No. 081919.